

# **Three-dimensional flow in cavity with elevated helicity driven by parallel walls**

**Alex Povitsky**

Professor, AIAA Associate Fellow, Email: povitsky@uakron.edu

Department of Mechanical Engineering, University of Akron, Akron, OH 44325-3903 USA

## **Abstract**

The proposed flow in a 3-D cubic cavity is driven by its top and bottom walls moving in perpendicular directions. This flow is a representative of genuinely three-dimensional highly separated vortical flows with elevated helicity yet having simple single-block cubical geometry of computational domain. The elevated level of helicity in the proposed flowfield is caused by motion of a wall in the direction of axis of primary vortex created by a parallel wall. The flowfield is obtained numerically by using second-order upwind scheme and  $200^3$  grid. Helicity, momentum and patterns of vortices are evaluated for the range of Reynolds numbers from 100 to 1000. Formation of two primary vortices with their axis oriented perpendicularly and patterns of secondary vortices are discussed. Computational results are compared to the well-known 3-D recirculating cavity flow case where the lid moves in the direction parallel to the cavity side walls. Also results are compared to the diagonally top-driven cavity and to cavity flow driven by moving top and side walls. The streamlines for the proposed flow show formation of two primary vortices with perpendicular axis so as the particles emerging from top and bottom of cavity do mix well.

## **Introduction**

This study introduces a simple geometry model of genuinely three-dimensional flow in cubical enclosed cavity with its top and bottom walls moving in orthogonal directions (Case A in Fig. 1) and studies the created flowfield as a function of the Reynolds number. Compared to prior set-ups of recirculating flow in driven cavity, the proposed flowfield has elevated helicity, sustained primary vortices with orthogonal axis of rotation, and two-sided mixing.

According to Ref.[1], internal recirculating cavity flows generated by the motion of one or more of the containing walls are not only technologically important, they are of great

scientific interest because they display almost all fluid mechanical phenomena in the simplest of geometrical settings. Driven cavity flows offer an ideal framework in which meaningful and detailed comparisons can be made between results obtained from experiment, theory, and computation [1]. The current study introduces and investigates novel recirculating cavity flow with elevated helicity and mixing. By [2], the scalar product of velocity and vorticity,  $\vec{u} \cdot \vec{\omega}$ , is defined as the helicity per unit volume of the flow. The level of helicity in the proposed flow set-up appears to be larger than those for prior cavity flow set-ups (Cases B and C in Fig. 1) because of elevated helicity at near-wall layer and in vortices.

Helicity plays an important role in characterizing complex three-dimensional flows including mixing, loss of stability and transition to turbulence (see [3] and references therein), vortex breakdown, the growth of magnetic fields in electrically-conducting fluids (see review [4] and references therein) and topology of vortices [5]. Helicity can lead to better mixing of chemical components in helical coherent structures (see [6] and references therein). The Arnold–Beltrami–Childress (ABC) [7] flow is a three-dimensional incompressible velocity field which is an exact solution of inviscid Euler equations in which helicity is the maximum (velocity and vorticity vectors are parallel). The ABC flow is a simple inviscid example of a fluid flow that can have chaotic trajectories and intense mixing associated with substantial helicity. This calls for the need to create a simple geometric set-up of viscous flow with elevated helicity.

In addition, helicity is used as a key variable in CFD algorithms and therefore benchmark flows in simple geometry can be used for verification of numerical methods. For example, Ref [8] suggested the use of helicity as an independent variable for numerical solution of vortex-dominated three-dimensional flows. Normalized helicity is used for visualization of vortices shed by air vehicles [9].

In the current study, the topology of vortices and level of helicity are compared to the widespread 3-D lid-driven cavity flow (Case C in Fig. 1) for which data are available [1]. Case C is the 3-D extension of the well-known 2-D lid-driven cavity flow benchmark. The prior studies [10] introduced flows in 2-D cavities in which the top and bottom walls move either in the same direction or in opposite direction with same velocity. However, for 2-D cavity flows vorticity is perpendicular to the cavity plane, velocity and vorticity are orthogonal and therefore helicity is equal to zero. For Case C, the velocity and vorticity are nearly orthogonal at each (y, z) plane except for the cavity ends and therefore the level of helicity appears to be low compared to new Case A.

The integral value of helicity for the proposed Case A is compared to that for the cubic cavity flow with diagonal symmetry in which the top wall moves along its diagonal (Case B-1 in Fig.1), Case B-1 was introduced by the author [11]. In fluids engineering, the Case B-1 flow set-up is important to model pneumatic transport of dusts [12] and to compute the degree of pollutant escape from the cavity according to various meteorological factors [13]. For verification and validation of numerical methods, the Case B flow set-up has been used to develop an artificial compressibility method for the incompressible Navier–Stokes equations [14], a preconditioned Krylov solver for stratified oceanic flows [15], multiple–relaxation–time Lattice-Boltzmann method, and to apply Lattice-Boltzmann methods to wall-bounded flows [16]. Ref [17] provides with numerical analysis of bifurcated flow for higher Re numbers for Case B-1 using  $100^3$  and  $200^3$  grids and second-order of accuracy finite volume code, OpenFOAM.

In Case B-1, the flow does impinge in the spatial angle formed by the front and a side wall. This leads to formation of the system of vortices caused by flow separation. As opposed to the widespread Case C, the flow is substantially three-dimensional for the entire cavity. It is

shown in the current study, that helicity in Case A is larger than that in Case B because the velocity in the  $z$  direction introduced by moving bottom is parallel to vorticity in the near-lid shear layer moving in the  $x$  direction and in the vortex created by moving cavity lid. Consequently, the integral of absolute value of helicity in Case A appears (see Section 3) more than doubled compared to that in Case B-1 for  $Re=1000$ .

Per Ref. [18], three-dimensional cavity flow with more than one moving wall does not appear in the literature. Ref [18] extends the 2-D cavity flow in three dimensions so as the top wall is moving to right, while the left vertical wall is moving down with the same constant velocity (see Fig.1, case B-2). In Case B-2, the flows recirculate in upper and lower cavity prisms separated by the cavity diagonal plane that forms plane of symmetry. Each recirculating flow does impinge in the spatial angle formed by the top and left walls. Integral of helicity appears to be comparable to case B-1. In Case B-2, the velocity component in the  $z$  direction is close to zero and substantial level of helicity appears only near the edge in which the flows impinge.

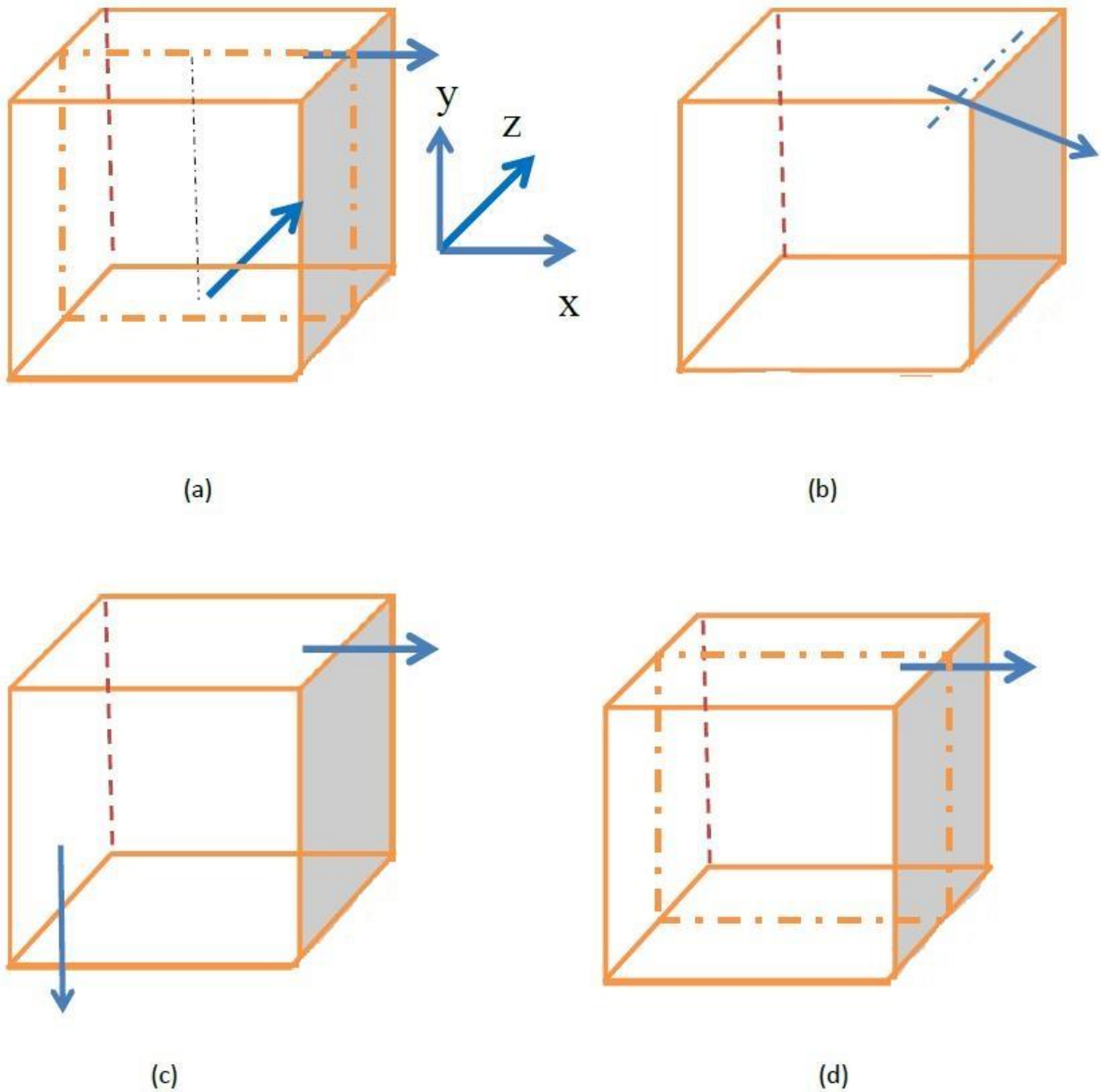


Figure 1: Flow in lid-driven cubical cavity: (a) top and bottom walls move in perpendicular directions (Case A), (b) top wall moves along its diagonal (Case B-1), (c) top wall moves along the x direction and the left wall moves down in the y direction (Case B-2), and (d) top wall moves along its edge (Case C)

The study is composed as follows. In Section 2, the mathematical model, boundary conditions, numerical method used, grid convergence and validation of approach are described.

In Section 3, flow pathlines and integrals of momentum and helicity for Cases A, B, and C are presented and discussed. In Section 4, local features of the flowfield including primary and secondary vortices are discussed comparatively for Cases A, B and C in order to evaluate the level of helicity. In Section 5, Conclusions are drawn.

## 2. Numerical method and grid convergence

The governing equations are the three-dimensional steady Navier-Stokes equations in Cartesian coordinates  $(x,y,z)$ . Unsteady version of the flow will be considered in the future research. The boundary conditions describe the no-slip and non-penetrating conditions at the steady and moving walls. Solutions depend on a single parameter named Reynolds number,  $Re=\rho UL/\mu$ , where  $\rho$  and  $\mu$  are density and viscosity of fluid, respectively,  $U$  is the speed of cavity lid,  $L$  is the length of cavity edge. For normalized variables used in the current study  $U$ ,  $L$  and  $\rho$  are taken equal to unity. Consequently,  $Re=1/\mu$ . Solutions were obtained for  $Re=100$ ,  $500$  and  $1000$ .

The 3-D cavity flow is studied by numerical solution of the three-dimensional viscous Navier-Stokes equations using ANSYS/Fluent finite-volume software with second-order upwind schemes for convective terms and second-order central scheme for viscous terms. ANSYS/Fluent software uses The Semi-implicit Method for Pressure-linked Equations (SIMPLE) [19] to resolve velocity and pressure coupling and algebraic multigrid (AMG) to solve the Poisson equation for pressure correction are used. After finite-volume discretization of continuity and momentum equations, conservation equation for a variable  $\phi$  at a finite volume (cell)  $P$  can be written as

$$a_p \phi_p = \sum_{nb} a_{nb} \phi_{nb} + b, \quad (1)$$

where  $a_p$  is the current finite-volume coefficient  $a_{nb}$  is the coefficient corresponding to a neighboring finite volume and  $b$  is a source term (mass imbalance term in equation for pressure correction in SIMPLE algorithm).

. After finite-volume discretization (1), large system of equations  $AX=B$  is developed. To reduce the computational time and ensure convergence of iterations, successive under- relaxation iterative method is used to solve the linear system, with relaxation coefficients 0.5 for pressure correction and 0.7 for momentum equations.

The stopping criteria are based on evaluation of residuals and their comparison to corresponding threshold values. Residual is a measure of an iterative solution convergence which evaluates the local imbalance of a conserved variable in each control volume (cell) [20] of the finite-volume grid. Residuals are summed over all finite-volume cells  $P$  and referred to as unscaled residuals:

$$R^\phi = \sum_{\text{cells } P} |\sum_{nb} a_{nb} \phi_{nb} + b - a_p \phi_p| \quad (2)$$

It is difficult to evaluate convergence by examining the residuals defined by the above equation since no scaling has been used. ANSYS Fluent scales the residuals using a scaling factor representing the magnitude of  $\phi$  through the domain:

$$R^\phi = \frac{\sum_{\text{cells } P} |a_{nb} \phi_{nb} + b - a_p \phi_p|}{\sum_{\text{cells } P} |a_p \phi_p|} \quad (3)$$

In this study, the convergence criteria for discretized mass and momentum equations have been assumed as  $R^\phi < 10^{-04}$ .

The uniform numerical grids with grid steps  $h=0.005$  ( $201 \times 201 \times 201$  grid) and  $h=0.01$  ( $101 \times 101 \times 101$  grid) are used. In Fig. 2, profiles of  $x$ -velocity component  $u$  in Case A along the vertical center-line of the cube ( $x=z=0.5$ ,  $0 \leq y \leq 1$ , see Fig 1a) are compared for computations with grid steps  $h=0.005$  and  $h=0.01$ . The results are quite similar for these two grids. At  $Re=1000$ , there is slightly more pronounced local minimum of velocity for more refined grid with  $h=0.005$ . This is explained by a smaller amount of numerical viscosity added by computations on a more refined grid.

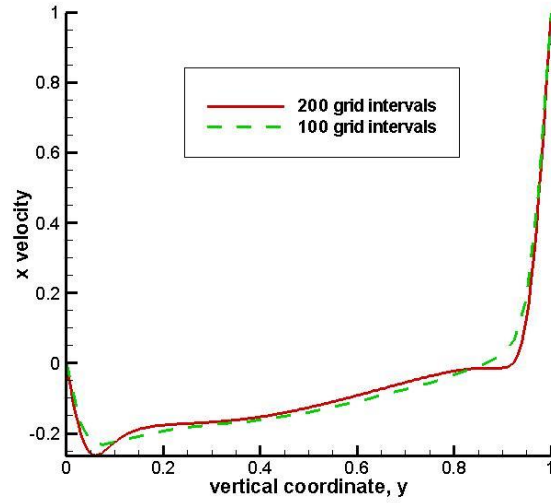
For the benchmark Case C, solution in Fig. 3 practically coincides with prior solutions (see Ref. [21], Fig. 5 and Ref. [22], Fig. 7). In turn, solutions [21] correspond to prior numerical [23] and experimental [24] results. Ref [21] used uniform mesh up to  $101 \times 101 \times 41$  points with symmetric boundary condition. This prior study (see Table 1, Ref [21]) studied grid convergence on coarser grids to accept the  $101 \times 101 \times 41$  grid with symmetry boundary condition at  $z=0.5$ , which corresponds to  $101 \times 101 \times 81$  finite-volume cells for the entire cavity.

Note that the 2-D lid-driven cavity flow (that is, cavity with infinite span in the  $z$  direction) has qualitatively similar velocity profile; however, the minimum of  $u$  component of velocity along the vertical centerline is more pronounced in the 2-D case reaching  $-0.38$  [25, Table 1].

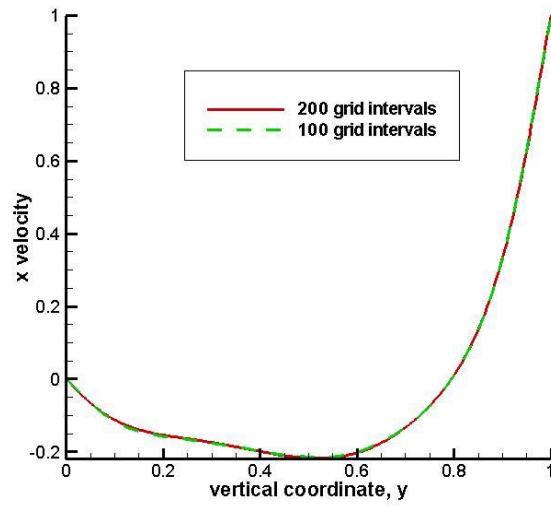
Comparison of  $u$ -velocity profile for Cases A and C along the cavity centerline show that profiles are qualitatively similar. In Case A, the maximum of recirculating velocity is located more close to the cavity bottom (that is,  $y=0$ ) compared to Case C. The upper boundary of recirculating zone ( $u=0$ ) is more close to the cavity top in Case A. Nevertheless, the  $z$ - velocity w



introduced by the moving bottom in Case A make the 3-D flowfield quite different compared to that in prior Cases B and C as shown in next sections.

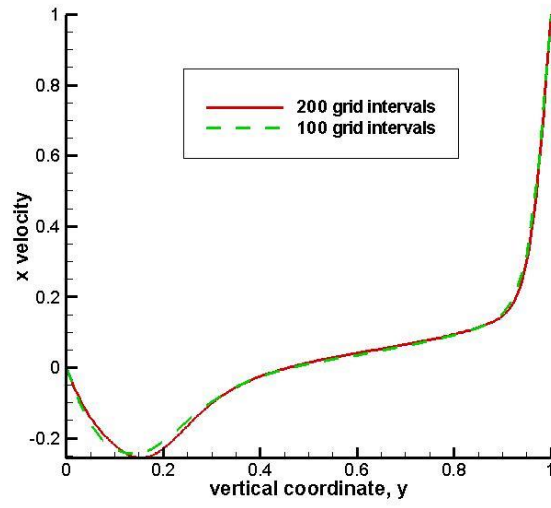


(a)  $Re=1000$

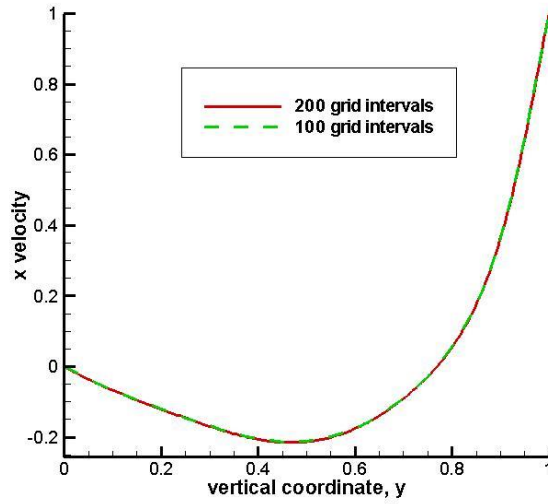


(b)  $Re=100$

Figure 2: Distribution of u-component of velocity along the cavity centerline: (a)  $Re=1000$  and (b)  $Re=100$ .



(a)



(b)

Figure 3: Benchmark Case C: x-component of velocity along the center line: a)  $Re=1000$  and b)  $Re=100$ .

### 3. Integral properties of flowfield

Table 1 shows the integral of momentum in the x direction for Cases A and C

$$I_T = \frac{1}{V} \int_V M_T, \quad (4)$$

where  $M_T = 0.5u^2$ . The amount of momentum for Cases A and C is similar. In both cases the integral of momentum somewhat decreases with the increase of Re. The magnitude of helicity (see Table 2) is defined as the integral of the magnitude of helicity density,  $h$ , which is the inner product of velocity and vorticity:

$$I_T = \frac{1}{V} \int_V |h|, \quad (5)$$

where  $h = \vec{u} \cdot \vec{\omega}$ .

The magnitude of helicity density is integrated to sum fluctuations of different sign of the local helicity density. The minimum level of helicity is observed in Case C. The maximum level of helicity is in the new proposed Case A. For Re=1000, Cases B-1 and B-2 have more than doubled level of helicity compared to the baseline Case C. It will be shown in the next section that the helicity in Cases B1 and B2 is substantial only at the areas of flow impingement. For Cases B and C there is no substantial velocity in the direction of vorticity.

On the contrary, for the proposed Case A the moving bottom wall introduces the velocity component  $z$  that forms the non-zero helicity (Eq. (5)) by the inner product of velocity with vorticity created by the top wall moving in the  $x$  direction (Fig 4a). In turn, the moving bottom wall, through the shear stress, generates vorticity oriented in the  $x$  direction. Multiplying by the velocity component,  $u$ , this vorticity component contributes to helicity. As a result, the magnitude of helicity in Case A is  $\sim 5$  times larger than that in Case C if Re=1000 (see Table 2). The difference in magnitude of helicity between Cases A and C does increase with the value of

Reynolds number (see Table 2). Details regarding local value of helicity per unit volume and normalized helicity (angle between  $\vec{u}$  and  $\vec{\omega}$ ) are presented in the next Section.

Table 1. Momentum in the x direction

Reynolds number	Case A	Case C
Re=100	0.0337	0.0374
Re=500	0.0260	0.0263
Re=1000	0.0215	0.0253

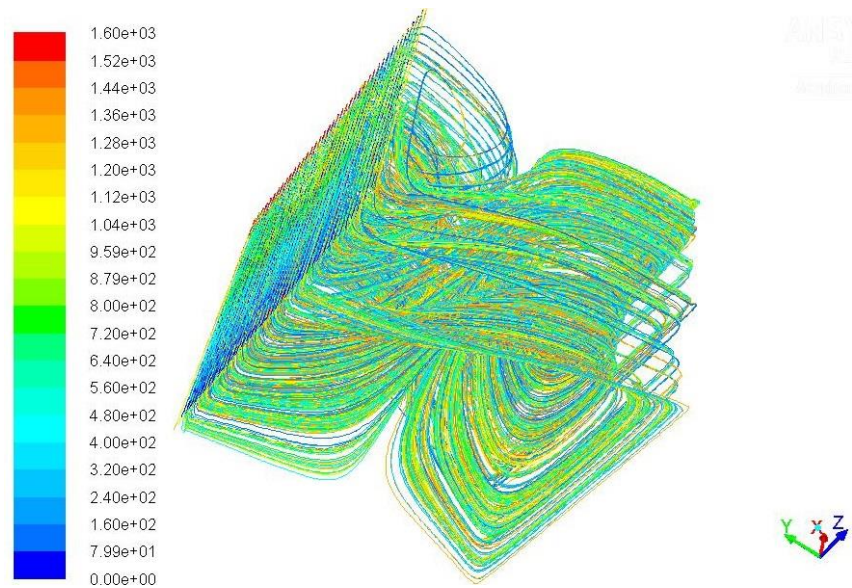
Table 2. Magnitude of helicity

Reynolds number	Case A	Case B-1	Case B-2	Case C
Re=100	0.0778	0.224	0.0798	0.0475
Re=500	0.3076	0.2025	0.1468	0.0580
Re=1000	0.3899	0.1756	0.1614	0.0798

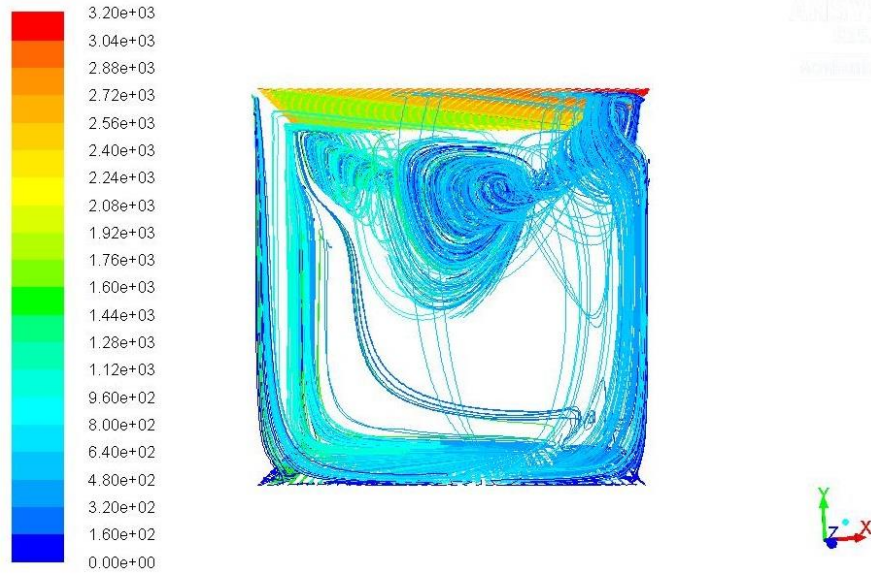
To visualize the flowfield, the pathlines for Case A are depicted in Fig. 4a. The total 1600 particles are traced; of them the first 800 particles are ejected from the bottom surface and the remaining 800 particles are ejected from the top surface. These pathlines are colored by the particle number. Two primary vortices are clearly seen in Fig.4a: the upper one with its axis oriented in the z direction and the lower one with its axis oriented in the x direction. Pathlines created by particles ejected from top and bottom surfaces are mixed well with each other: red and yellow pathlines corresponding to particles ejected from the top surface are mixed with blue and green pathlines corresponding to particles ejected from the bottom surface. Particles, which are ejected from bottom and top walls, participate in the swirling motion to the same degree. This indicates the uniform involvement of material into swirling motion and mixing in Case A.

The pathlines in Case B-1 are depicted in Fig. 4b. The vortex tube is oriented in the  $(x, -z)$  direction parallel to the direction of moving lid (see Fig. 1b). The vortex tube is bended so as it nearly touches the upper wall at its edges and is deflected down toward the cavity center. The bended shape of vortex tube creates numerous secondary vortices of lesser strength as detailed in the prior study by the author [11]. The first 1600 particles are ejected primarily from the bottom and the other 1600 particles are ejected from the top. The blue and green color of pathlines indicates that most of material involved in swirling motion is ejected from the bottom.

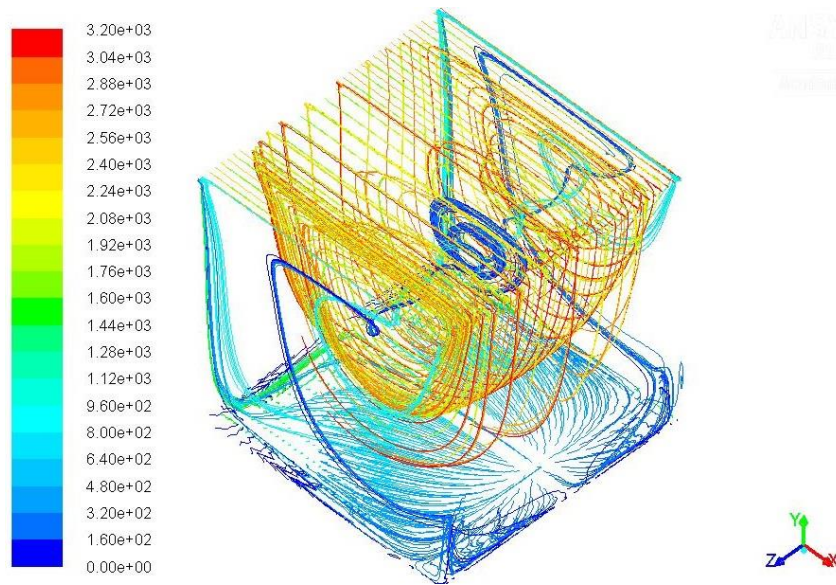
In Case C, pathlines form primary vortex with its axis oriented in the  $x$  direction. Yellow and red colors of pathlines indicate that most of material involved in swirling motion is ejected from the top with the exception of blue pathlines of particles ejected from bottom, which enter the vortex through its edges and move toward center of cavity.



(a)



(b)

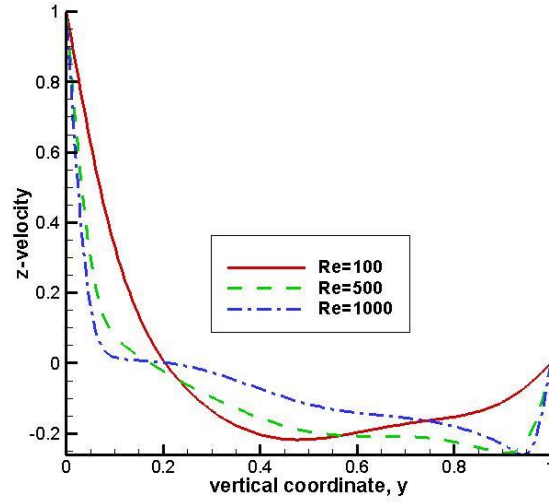


(c)

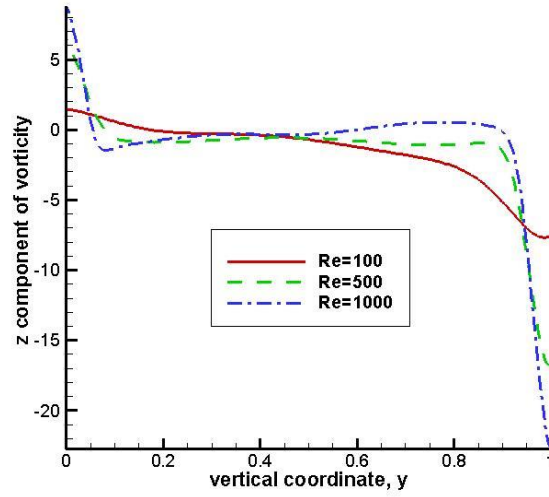
Figure 4: Pathlines colored by particle number ejected from bottom and top surfaces: (a) Case A, (b) Case B-1, and (c) Case C.

#### 4. Local flowfield and distribution of helicity

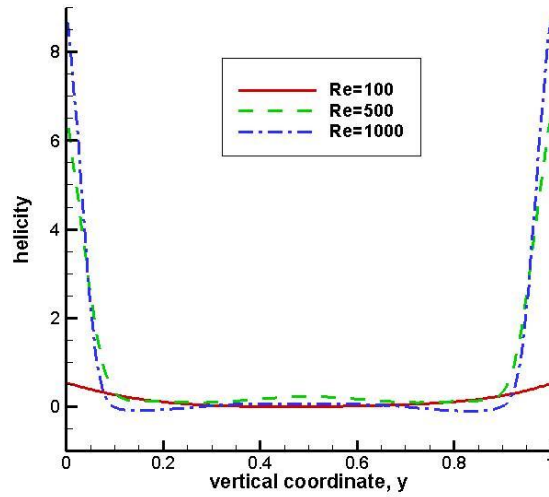
In Figure 5a, b, z-components of velocity and vorticity are plot along the cube centerline (see Fig. 1a). The centerline is located outside of vortex tubes (see vertical cross-sectional vector field, Fig. 6); therefore, the distribution of helicity is dominated by shear layers caused by moving top and bottom walls. The z component of velocity,  $w$ , along the cube centerline is a mirror reflection of the  $u$  component with respect to  $y=0.5$  (compare Fig. 5a and Fig. 2a). The recirculating zone ( $w<0$ ) is formed in the upper part of the cavity. For  $Re=100$ , the near-wall layers dominated by moving walls are somewhat wider compared to those for  $Re=500$  and  $1000$ .



(a)



(b)



(c)

Figure 5: Case A: centerline profiles of (a) z component of velocity, (b) z-component of vorticity and (c) magnitude of helicity

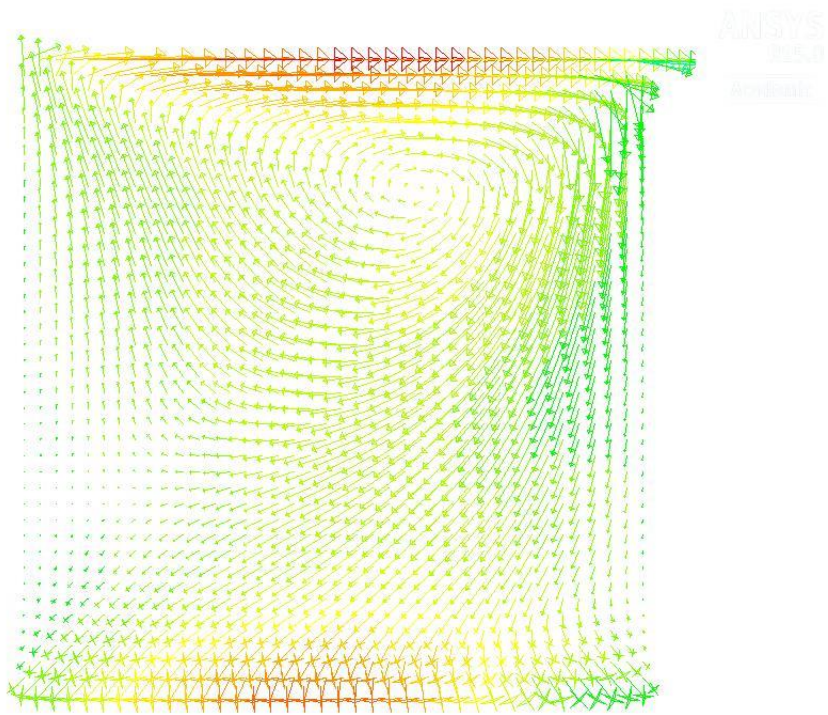
Velocity vector field colored by helicity density,  $h$ , is plot in vertical cross-section ( $z=0.5$ ) and shown in Figs. 6a, b, c for  $Re=100$ , 500 and 1000, in correspondence. The velocity vector flowfield for Case C ( $Re=1000$ ) is presented in Fig. 6d for comparison. The primary vortex is created by the top of the cavity moving in the positive  $x$  direction. The shear stress is



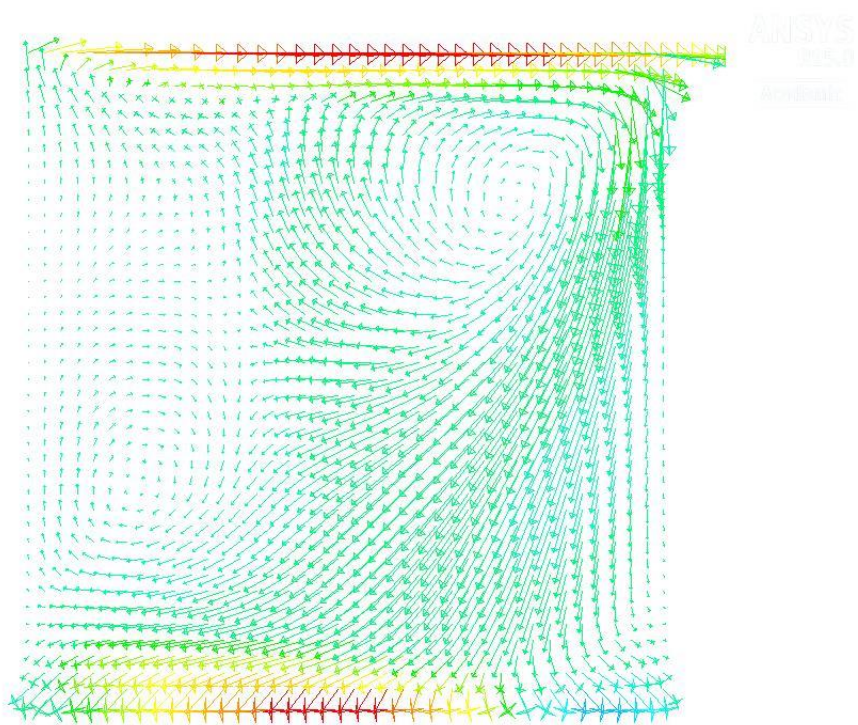
applied to the upmost layer of fluid that causes its motion in the x direction. The right wall blocks the forward motion of fluid and turns it toward the bottom in Case C. In Case A, formation of vortex by motion of the bottom wall in the z direction deflects the bottom-moving fluid toward the diagonal of cross-section.

In Case A ( $Re=500$  and  $1000$ ), the secondary co-rotating vortex is formed above the impinging flow near the lower part of right wall, see Fig. 6 b, c. For  $Re=100$  (Fig. 6a), the low velocity magnitude flow region is formed in place of secondary vortex.

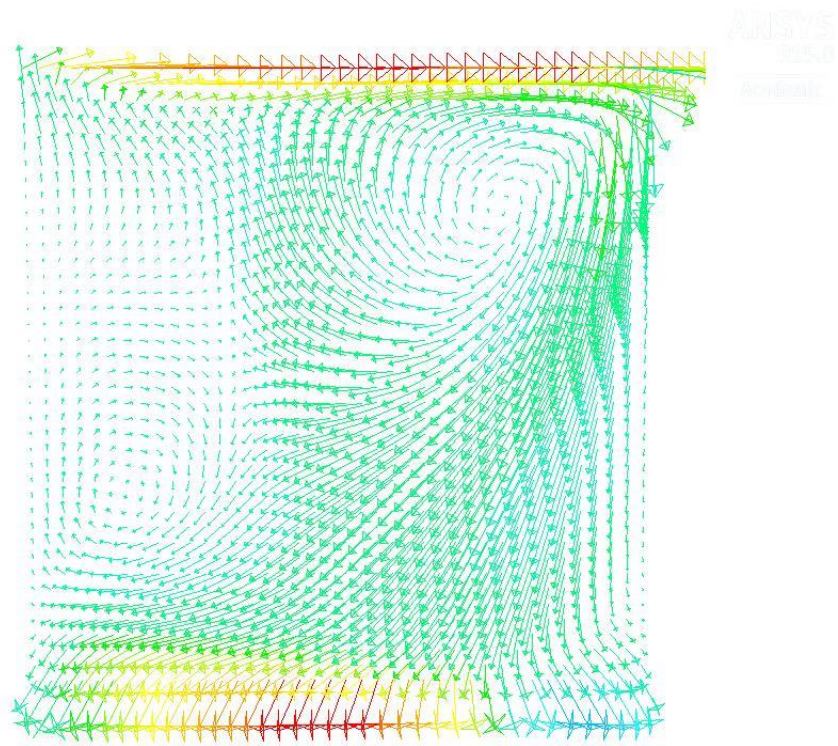
In Case C, the fluid moving toward bottom form a secondary counter-rotating vortex near the bottom right corner (compare Figs 6a,b,c to Fig. 6d). In Case C (Fig. 6d), the geometry is an extension to three dimensions of the 2-D lid-driven square cavity in which the secondary vortices are located at near-bottom corners. When the Reynolds number increases, the corner eddies grow larger [26]. This vortex is not observed in Case A (Fig 6a, b, c) being convected downstream by the flow in the z direction.



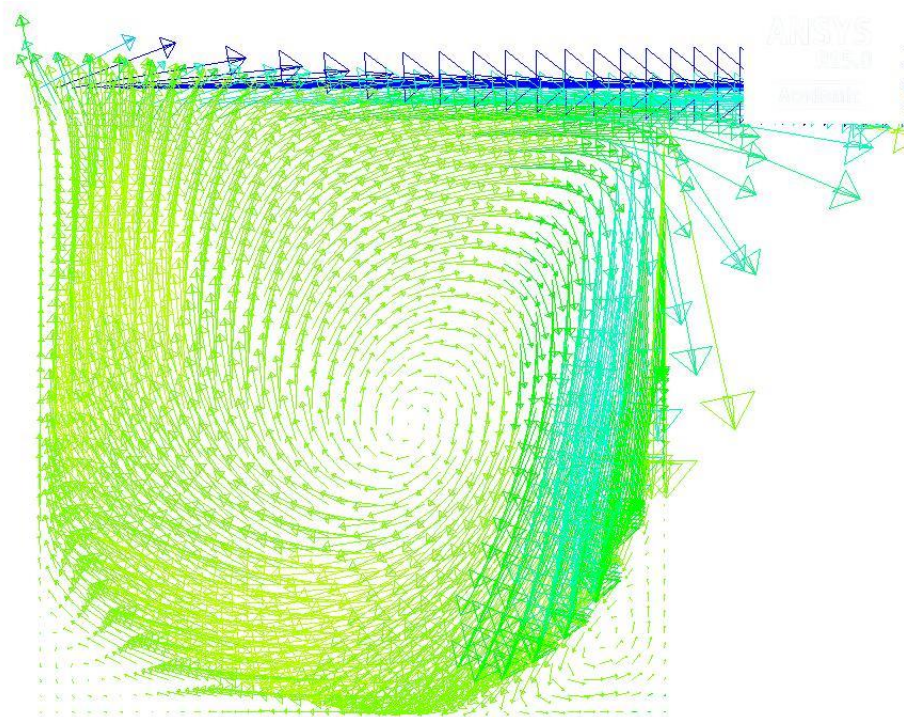
(a)



(b)



(c)



(d)



Figure 6: Velocity vector field colored by helicity density,  $h$ , in vertical cross-section ( $z=0.5$ ) for (a)  $Re=100$  ( $h$  from -1.68 to 1.68) (b)  $Re=500$  ( $h$  from -3.78 to 5.67), (c)  $Re=1000$  ( $h$  from -3.78 to 5.68), and (d) for Case C ( $Re=1000$ ) ( $h$  from -0.01 to 0.01)

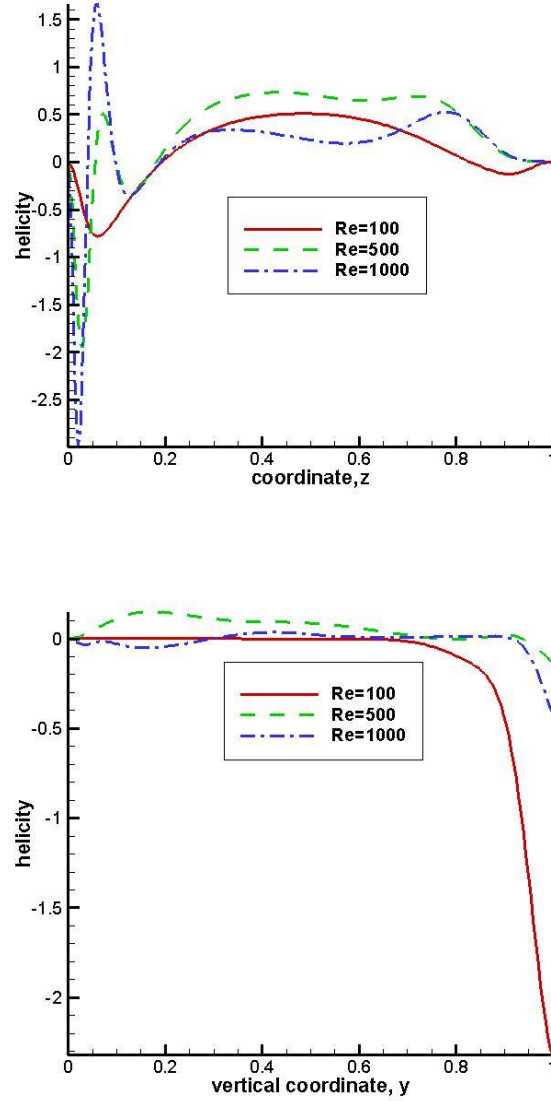


Fig 7: Helicity density in Case B-1: (a) along near-edge line and (b) along the vertical centerline

In Fig. 7a, helicity density,  $h$ , is plot along the horizontal line ( $x=y=0.95$ ) parallel to upper right cavity edge (Fig. 1b). In Case B-1, the lid-driven flow impinges into upper right corner ( $z=0$ ) in Fig. 1b. The magnitude of helicity in Fig. 7a is below 0.5 except for impingement area ( $z < 0.1$ ) at which the magnitude of  $h$  reach  $\sim 3$  for  $Re=1000$ . In Fig. 7b, helicity is plot along

the cube centerline in Case B-1. Maximum magnitude of helicity near the cavity top is  $\sim 0.3$  for  $Re=1000$ .

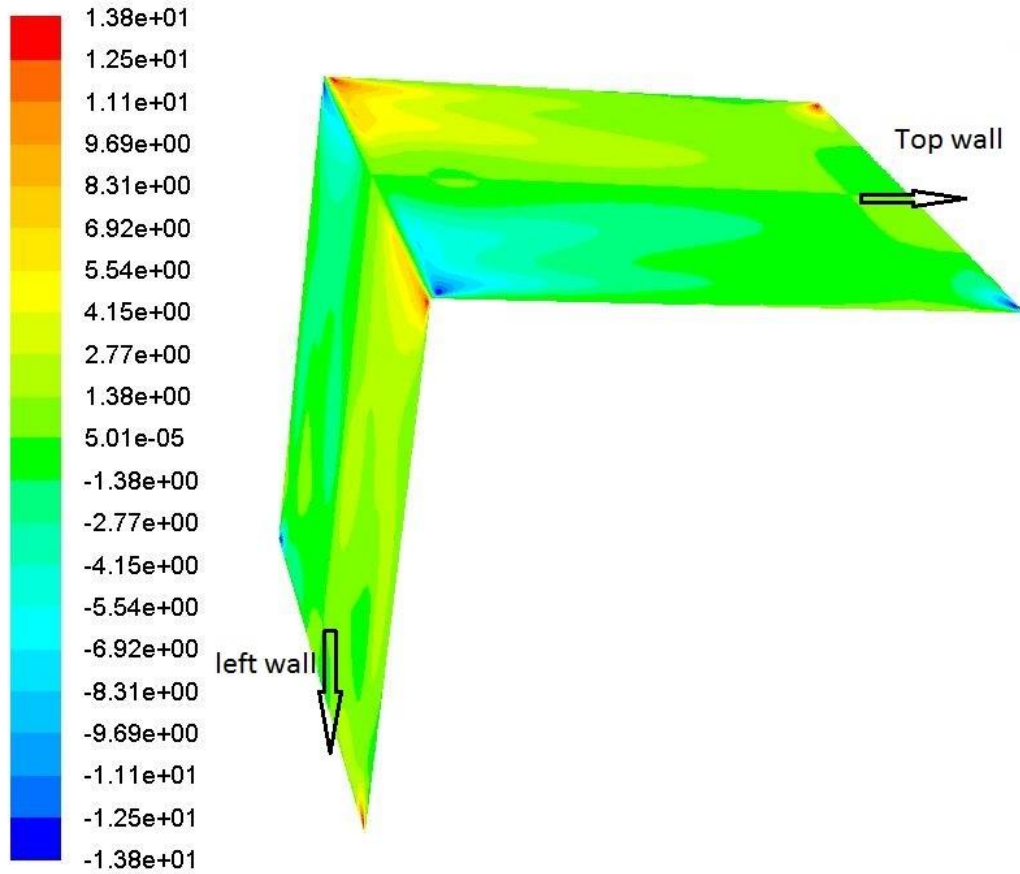


Fig 8: Helicity in Case B-2

In Figure 8, helicity density,  $h$ , is plot at the top and left cavity walls to show the areas of elevated helicity in Case B-2. For the rest of the cavity flow the helicity is close to zero except for areas located near the corners about which left and top walls move. In summary, the level of helicity in Cases B-1 and B-2 are much smaller compared to Case A (see Fig. 5c).

How helical a flow is, can be evaluated using the normalized (relative) helicity corresponding to the degree of alignment of the velocity and vorticity [6]:

$$\cos(\alpha) = h/(\overline{\mathbf{u}} \cdot \overline{\boldsymbol{\omega}}) \quad (6)$$

The value of  $\cos(\alpha)$  is close to 1 when vectors of velocity and vorticity are parallel and close to -1 when they are antiparallel. The value of  $\cos(\alpha)$  is close to zero when velocity and vorticity are non-aligned. Flow situations in which the magnitude of normalized helicity is close to unity is important in dynamics of vortices and turbulence [4]. The flowfield in Case A naturally has such areas of flowfield because the motion of each one of walls (top or bottom) creates velocity field aligned with the vortex axis created by another parallel wall.

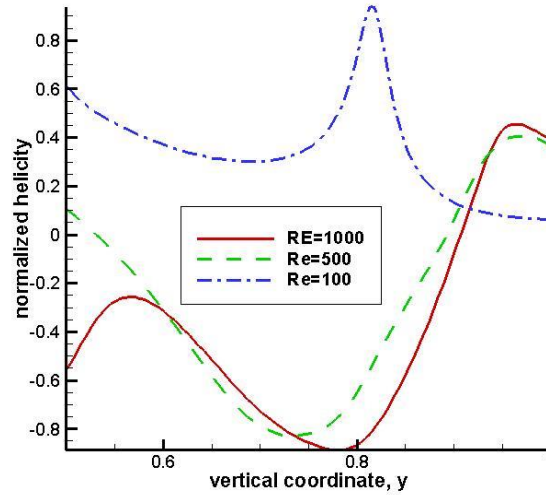
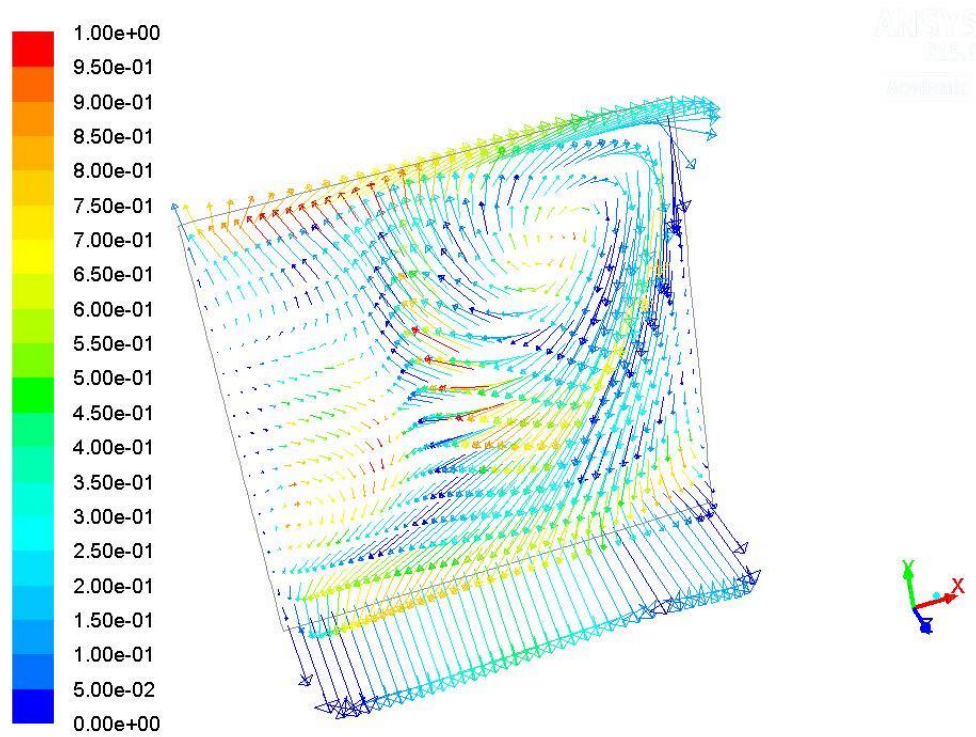


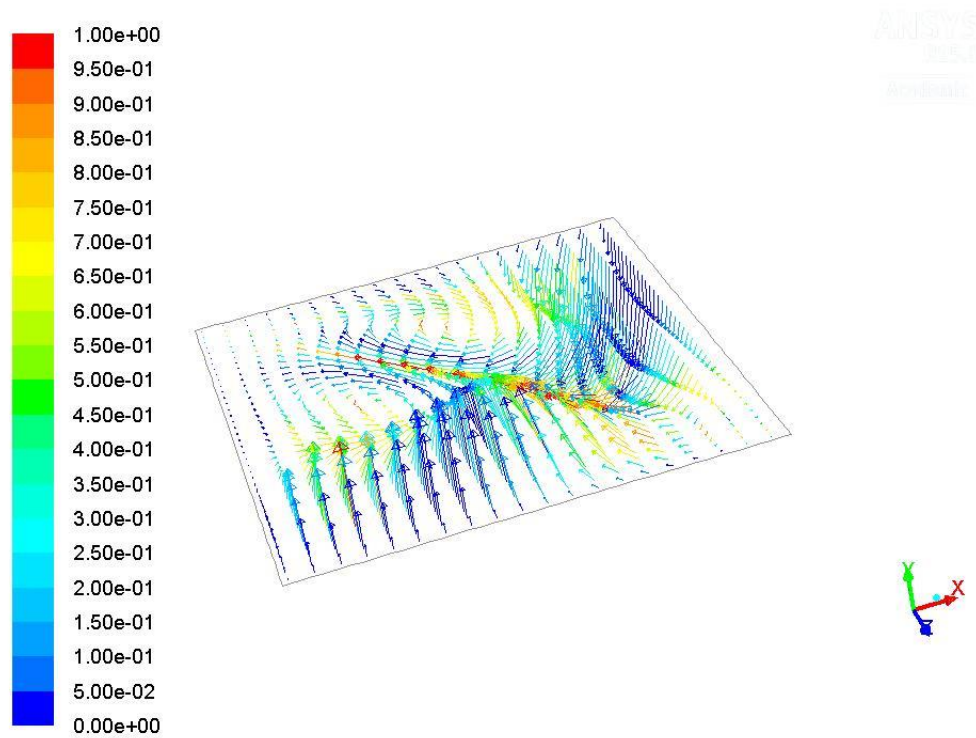
Figure 9: Normalized helicity in Case A. Normalized helicity is plot along vertical lines ( $z=0.5$ ) that passes through the vortex center ( $x=0.65$  for  $Re=1000$ ,  $x=0.72$  for  $Re=500$ , and  $x=0.626$  for  $Re=100$ )

In Figure 9, the magnitude of normalized helicity,  $|\cos(\alpha)|$ , is plot along vertical lines,  $0.5 \leq y \leq 1$ . Each line passes through the vortex center ( $x=0.65$  for  $Re=1000$ ,  $x=0.72$  for  $Re=500$ , and  $x=0.626$  for  $Re=100$ ) at the middle of the cavity ( $z=0.5$ ). The graphs in Fig. 9 show that  $|\cos(\alpha)|$  exceeds 0.8 at the central part of each vortex. The sign of normalized helicity is

opposite for  $Re=100$  and for larger Reynolds numbers ( $Re=500$  and  $Re=1000$ ) because the sign of vorticity is opposite for these cases, see Fig. 5b. The normalized vorticity plots show that the maximum magnitude of normalized helicity is reached at core of vortices while the maximum magnitude of helicity density corresponds to near-wall layer (Fig. 5c).



(a)



(b)

Figure 10: Velocity vector field colored by magnitude of normalized helicity: (a) central vertical plane,  $z=0.5$  and (b) middle horizontal plane,  $y=0.5$ .

To show elevated level of normalized helicity at vortices, the velocity vector field colored by magnitude of normalized helicity is shown at central vertical plane (Fig. 10a) and at middle horizontal plane (Fig. 10b). The vortical areas do show an elevated level of normalized helicity.

## Conclusions

The proposed flow in 3-D cubic cavity is driven by its top and bottom walls moving in perpendicular directions. This flow is a representative of genuinely three-dimensional highly separated vortical flows yet having simple single-block cubical geometry of computational domain.



To obtain the flowfield, the governing incompressible Navier-Stokes equations are solved numerically using second-order upwind scheme for convective terms and second-order central scheme for viscous terms. Solutions obtained on  $100^3$  and  $200^3$  grids show close proximity to each other for both Cases A and C. To validate the numerical method, solutions in Case C are practically identical to those known in literature. The  $200^3$  grid is therefore used in numerical modeling in the current study.

The proposed flow is compared to flows characterized by a diagonal plane of symmetry (Cases B-1 and B-2). The streamlines for the proposed flow show formation of two primary vortices with perpendicular axis. The particles emerging from top and bottom appear to mix well. This differs the proposed flow from the well-known benchmark Case C in which the particles emerging from the top were primarily involved in circulating motion and from the Case B-1 in which particles emerging from the bottom are chiefly involved in circulating motion. For proposed flowfield, secondary vortices are created for  $Re > 100$  and located quite differently from those in the benchmark Case C.

Helicity is quantified as an inner product of vorticity and velocity and is considered as an important measure of transition to turbulence and degree of mixing. The elevated level of helicity in the proposed flowfield is caused by the motion of a wall (either top or bottom) in the direction of vorticity created by another moving parallel wall. The vorticity is created by viscous shear stress caused by moving wall and by vortex created by no-penetration effect of stationary side walls, which block the shear flow in the direction of moving wall. For  $Re = 1000$ , helicity is five times bigger for the proposed flow compared to flow driven by the cavity lid (Case C). For cavity flows driven by lid moving along its diagonal (Case B-1) and by two perpendicular walls (Case B-2), the helicity is approximately two times smaller compared to Case A. For Case B

flows, the elevated helicity level is limited to the corners of the cavity where the driven flow impinges into walls. For the proposed Case A flow, the helicity is elevated in the spatial areas next to moving top and bottom walls ( $y < 0.1$  and  $y > 0.9$ ) while the magnitude of normalized helicity ( $\cos$  of angle between  $\vec{u}$  and  $\vec{\omega}$ ) is close to unity within flow vortices.

## References

1. P. N. Shankar and M. D. Deshpande, Fluid Mechanics in the Driven Cavity, Annual Review of Fluid Mechanics, Vol. 32, pp. 93-136, 2000.
2. H.K. Moffatt, The degree of knottedness of tangled vortex lines, J. Fluid Mech. ,1969, Vol. 35, part 1, pp. 117-129.
3. A. Tsinober, The Essence of Turbulence as a Physical Phenomenon, Springer, 2014.
4. H.K. Moffatt and A. Tsinober, Helicity in Laminar and Turbulent Flow, Annual Review of Fluid Mechanics, 1992, Vol. 24, pp. 281-312.
5. M. W. Scheelera, D. Klecknera, D. Proment, G. L. Kindlmann, and W. T. M. Irvine, Helicity conservation by flow across scales in reconnecting vortex links and knots, Proceedings of the National Academy of Science (PNAS), Vol. 111, No. 43, pp. 15350–15355, 2014, [www.pnas.org/cgi/doi/10.1073/pnas.1407232111](http://www.pnas.org/cgi/doi/10.1073/pnas.1407232111).
6. A. Pouquet and P.D. Minni, The interplay between helicity and rotation in turbulence: implications for scaling laws and small-scale dynamics, Phil. Trans. R. Soc. A (2010) 368, 1635–1662.
7. V. I. Arnold and B. A. Khesin, Topological Methods in Hydrodynamics, Springer-Verlag, 1998.

- 
8. M. A. Olshanskii and L. G. Rebholz, Velocity–vorticity–helicity formulation and a solver for the Navier–Stokes equations, *Journal of Computational Physics*, Vol. 229 (2010), pp. 4291–4303.
  9. Y. Levy, D. Degani, and A. Seginer, Graphical Visualization of Vortical Flows by Means of Helicity, *AIAA J.*, Vol. 28(8), pp. 1347-1352, 1990.
  10. S. Arun and A. Satheesh, Analysis of flow behavior in a two sided lid driven cavity using Lattice Boltzmann technique, *Alexandria Engineering Journal*, Vol. 54, 2015, pp. 795–806.
  11. Povitsky A., Three-dimensional flow in cavity at yaw, *Nonlinear Anal. Theory Methods Appl.* 63, e1573–e1584 (2005). Preliminary versions: AIAA Paper 2847-2001 (2001), Tech. Rep. 211232, NASA/CR (2001), ICASE Report No. 2001-31.
  12. P. Kosinski, A. Kosinska, and A.C. Hoffmann, Simulation of solid particles behavior in a driven cavity flow, *Powder Technology*, Volume 191, Issue 3, 2009, pp. 327–339.
  13. Y.-H. Ryu and J.-J. Baik, Flow and dispersion in an urban cubical cavity, *Atmospheric Environment*, Vol. 43, Issue 10, 2009, pp. 1721–1729.
  14. P. Asinari, T. Ohwada, E. Chiavazzo, and A. F. Di Rienzo, Link-wise artificial compressibility method, *Journal of Computational Physics*, Vol. 231, Issue 15, 2012, pp. 5109–5143.
  15. S.A. Melchior, V. Legat, P. van Dooren, and A.J. Wathen, Analysis of preconditioned iterative solvers for incompressible flow problems, *International Journal for Numerical Methods in Fluids*, Vol. 68 (3), pp. 269-286, 2012.
  16. R. K. Freitas, A. Henze, M. Meinke, and W. Schröder, Analysis of Lattice-Boltzmann methods for internal flows, *Computers & Fluids*, Vol. 47, Issue 1, 2011, pp. 115–121

- 
17. Y. Feldman, Theoretical analysis of three-dimensional bifurcated flow inside a diagonally lid-driven cavity, *Theoretical and Computational Fluid Dynamics*, Vol. 29, Issue 4, pp. 245-261, 2015.
  18. B. B. Beya and T. Lili, Three-dimensional incompressible flow in a two-sided non-facing lid-driven cubical cavity, *C. R. Mecanique*, Vol. 336, p. 863, 2008.
  - 19 Patankar, S. Numerical heat transfer and fluid flow. CRC press, 1980.
  20. ANSYS Fluent guide, ANSYS Inc., Version 15, PDF Documentation, 2015.
  21. G. Guy and F. Stella, A Vorticity-Velocity Method for the Numerical Solution of 3D Incompressible Flows, *Journal of Computational Physics*, Vol. 106, pp 286-289, 1993.
  22. J.-Y. Yang, S.-C. Yang, Y.-N. Chen,y and C.-A. Hsu, Implicit Weighted ENO Schemes for the Three-Dimensional Incompressible Navier–Stokes Equations, *Journal of Computational Physics*, Vol. 146, pp. 464–487, 1998.
  23. H.C. Ku, R.S. Hirsch and T. Taylor, *Journal of Computational Physics*, Vol. 70, p. 439, 1987.
  24. J. R. Koseff and R. L. Street, *ASME J. of Fluids Eng.*, Vol. 106, p. 390, 1984.
  25. U. Ghia, K,H, Ghia and C.T.Shin, High-Re Solutions for Incompressible Flow Using the Navier-Stokes Equations and a Multigrid Method, *Journal of Computational Physics*, Vol.48, pp. 387-411, 1982.
  26. Schreiber, R. and Keller, H.B. Driven cavity flows by effective numerical techniques, *Journal of Computational Physics*, Vol. 49, p. 310, 1983.